Appl. Phys. B 87, 363–372 (2007)
DOI: 10.1007/s00340-007-2585-y

Applied Physics B
Lasers and Optics

K.J. DAUN[1,✉]
B.J. STAGG[2]
F. LIU[1]
G.J. SMALLWOOD[1]
D.R. SNELLING[1]

Determining aerosol particle size distributions using time-resolved laser-induced incandescence

[1] National Research Council of Canada, Ottawa, K1A 0R6, Canada
[2] Columbian Chemicals Company, 1800 West Oak Commons Ct., Marietta, GA 30062, USA

Received: 30 August 2006/Revised version: 18 December 2006
Published online: 17 February 2007 •

ABSTRACT The particle size distribution within an aerosol containing refractory nanoparticles can be inferred using time-resolved laser-induced incandescence (TR-LII). In this procedure, a small volume of aerosol is heated to incandescent temperatures by a short laser pulse, and the incandescence of the aerosol particles is then measured as they return to the ambient gas temperature by conduction heat transfer. Although the cooling rate of an individual particle depends on its volume-to-area ratio, recovering the particle size distribution from the observed temporal decay of the LII signal is complicated by the fact that the LII signal is due to the incandescence of all particle size classes within the sample volume, and because of this, the particle size distribution is related to the time-resolved LII signal through a mathematically ill-posed equation.

This paper reviews techniques proposed in the literature for recovering particle size distributions from TR-LII data. The characteristics of this problem are then discussed in detail, with a focus on the effect of ill-posedness on the stability and uniqueness of the recovered particle size distributions. Finally, the performance of each method is evaluated and compared based on the results of a perturbation analysis.

PACS 44.05.+e; 47.70.Pq; 78.70.-g; 65.80.+n; 78.20.Ci

1 Introduction

Techniques for measuring particle size distributions in aerosols are important in many applications. For example, they are essential for establishing the impacts of anthroporgenically-generated soot particles on human health [1] and the ecosystem [2], which are both strong functions of particle size. The size of primary particles in soot aggregates also has a pronounced effect on radiation heat transfer in engines and furnaces [3], so determining particle morphology within these devices is paramount when optimizing their performance. Finally, accurate particle size measurement is a critical part of engineered nanoparticle synthesis [4].

Since its introduction by Melton [5], time-resolved laser-induced incandescence has evolved into a powerful tool for making in situ property measurements of aerosol dispersions including the particle size distribution. In this procedure, a laser pulse heats a small sample volume of aerosol to temperatures substantially higher than the ambient gas temperature, typically 3000–3500 K in particle-sizing experiments. The particles then cool to the ambient gas temperature in microseconds, primarily by conduction to the surrounding gas. If sublimation and radiant heat loss effects are negligible, which is usually the case in low-fluence experiments, the particle temperatures are governed by

$$\varrho c \frac{\pi d_\mathrm{p}^3}{6} \frac{\mathrm{d}T_\mathrm{p}(t, d_\mathrm{p})}{\mathrm{d}t} = q_\mathrm{in}(t, d_\mathrm{p}) - q_\mathrm{cond}(t, d_\mathrm{p}) \,, \tag{1}$$

where ϱ and c are the particle density and specific heat, $q_\mathrm{in}(t, d_\mathrm{p})$ is the energy absorbed by the particle during the excitation laser pulse, and $q_\mathrm{cond}(t, d_\mathrm{p})$ is the conduction heat loss from the particle to the surrounding gas. (The dependence of ϱ and c on particle temperature is omitted from (1) for clarity, but is accounted for in the analysis later in the paper.) If the excitation laser operates at a wavelength λ_e, the rate of laser energy absorption by the particle is given by

$$q_\mathrm{in}(t, d_\mathrm{p}) = F_0 \, q(t) \, Q_{\mathrm{abs},\lambda_\mathrm{e}}(d_\mathrm{p}) \frac{\pi d_\mathrm{p}^2}{4} \,, \tag{2}$$

where F_0 is the total laser fluence and $q(t)$ is the laser temporal power density. If the particle absorbs in the Rayleigh limit (i.e., $\pi d_\mathrm{p}/\lambda_\mathrm{e} < 0.3$ [6]), the particle absorption efficiency is equal to $Q_{\mathrm{abs},\lambda_\mathrm{e}}(d_\mathrm{p}) = 4\pi d_\mathrm{p}/\lambda_\mathrm{e} E(\boldsymbol{m}_{\lambda_\mathrm{e}})$, where $E(\boldsymbol{m}_{\lambda_\mathrm{e}})$ is the absorption function of the complex index of refraction. This equation can also be applied to the primary particles of soot aggregates via Rayleigh–Debye–Gans polyfractal aggregate theory as long as the soot aggregate structure is sufficiently open and the primary particle diameters lie within the Rayleigh limit [7].

At atmospheric pressures, heat conduction from particles to the surrounding gas usually occurs within the free-molecular regime and is governed by [8]

$$q_\mathrm{cond}(t, d_\mathrm{p}) = \alpha_\mathrm{T} \frac{\pi d_\mathrm{p}^2}{4} \frac{P_\mathrm{g} \bar{c}(T_\mathrm{g})}{2T_\mathrm{g}} \frac{\gamma^* + 1}{\gamma^* - 1} [T_\mathrm{p}(t, d_\mathrm{p}) - T_\mathrm{g}] \,, \tag{3}$$

✉ Fax: 613 957 7869, E-mail: kyle.daun@nrc-cnrc.gc.ca

where α_T is the thermal accommodation coefficient, γ^* is obtained from

$$\frac{1}{\gamma^*-1}=\frac{1}{T_p(t,d_p)-T_g}\int_{T_g}^{T_p}\frac{dT}{\gamma(T)-1}, \tag{4}$$

and $\bar{c}(T_g)=\sqrt{8k_BT_g/\pi m_g}$, in which k_B is Boltzmann's constant and m_g is the molecular mass of the gas. (Although aggregate shielding effects are often important [9], they are neglected in this paper for simplicity.) Equations (1)–(3) can be solved for the temperature of a particle of diameter d_p at any time t after the peak temperature using standard numerical techniques.

Because the particle cooling rate is inversely proportional to the particle volume-to-surface area ratio, the observed incandescence decay rate is a function of the particle size distribution. At any instance in the cooling process, the spectral incandescence of the measurement volume at the detection wavelength λ is related to the size distribution through a Volterra integral equation of the first kind,

$$J_\lambda[t,\,f(d_p)]=C_\lambda\int_0^\infty f_d(d_p)K_\lambda(t,d_p)\,dd_p, \tag{5}$$

where $f_d(d_p)$ is the probability density function of the particle diameter and C_λ is a constant that depends on the particle volume fraction and the optical measurement system characteristics. The kernel of (5) is given by

$$K_\lambda(t,d_p)=E_{b,\lambda}(t,d_p)Q_{abs,\lambda}(d_p)\frac{\pi d_p^2}{4}, \tag{6}$$

where $E_{b,\lambda}(t,d_p)$ is the spectral emissive power of a blackbody at a temperature $T_p(t,d_p)$ and wavelength λ. Instead of relying on a single spectral incandescence measurement to determine the size distribution, many researchers measure the aerosol incandescence at two detection wavelengths and then calculate an effective temperature,

$$T_e[t,\,f(d_p)]=\frac{hc_0/k_B(1/\lambda_1-1/\lambda_2)}{\ln\left\{\dfrac{E(\boldsymbol{m}_{\lambda1})}{E(\boldsymbol{m}_{\lambda2})}\dfrac{J_{\lambda2}[t,\,f_d(d_p)]}{J_{\lambda1}[t,\,f_d(d_p)]}\left(\dfrac{\lambda_2}{\lambda_1}\right)^6\right\}}, \tag{7}$$

where h is Planck's constant and c_0 is the speed of light in a vacuum. Equation (7) is an implicit function of $f_d(d_p)$ through (5). Unlike spectral incandescence, the effective temperature is independent of both the volume fraction of particles contained within the aerosol measurement volume and their optical properties provided that $E(\boldsymbol{m}_{\lambda1})\approx E(\boldsymbol{m}_{\lambda2})$.

The spectral incandescence or effective temperature curve corresponding to a particular size distribution can be calculated directly from the above equations; we refer to this process as solving the mathematically well-posed forward problem. More often, however, the objective is to solve the inverse of this problem, i.e., to determine the size distribution that causes an experimentally observed J_λ or T_e decay. This procedure is relatively straightforward if particle sizes are assumed to be monodisperse, in which case all the particles have the same temperature decay curve and d_p can be found directly from the time constant. This procedure was first used by Will et al. [10] and Mewes and Seitzman [11] to determine an average primary particle size of a soot aerosol using TR-LII measurements.

In reality, however, particle sizes in most aerosols are polydispserse and $f_d(d_p)$ can only be found by solving (5) or (7). This is far more difficult because integral equations of the first-kind like (5) are mathematically ill-posed. The formal distinction between well-posed and ill-posed problems was first made by Hadamard [12], who defined well-posed problems as those that (i) have solutions (ii) that are both unique and (iii) stable under small perturbations in the problem definition or input data; problems that fail to satisfy any of the above criteria are deemed to be ill-posed. In this problem Hadamard's first criterion is satisfied since the observed incandescence decay is produced by at least one particle size distribution. There is, however, no guarantee that there is only one unique distribution that can produce the observed LII signal, and furthermore, a particle size distribution that satisfies (5) and (7) may be very sensitive to small perturbations in the incandescence data and modeling errors. The latter is a particular concern, since photodetector measurements are usually contaminated with substantial shot noise, and many of the physical parameters in the heat transfer model are not known with a high degree of certainty.

The above properties make ill-posed problems difficult to solve, so special mathematical techniques must be employed to recover the particle size distribution from time-resolved LII data. These techniques belong to one of two classes: explicit methods solve the ill-posed mathematical problem for the unknown parameter directly, usually by first transforming the integral equation into an ill-conditioned matrix equation that is then solved using regularization. Roth and Filippov [13] used this approach to solve (5) for $f_d(d_p)$ using an iterative regularization scheme [14, 15]. Although this method was demonstrated on a test problem having a known distribution, it has limited practical utility since the maximum and minimum particle sizes must be known with some accuracy to restrict the nullity of the coefficient matrix to a manageable level, which is rarely possible in most real-world applications.

Implicit methods, on the other hand, work by repeatedly substituting trial solutions of $f_d(d_p)$ into the forward problem, either (5) or (7), until the modeled variable, $J_\lambda^{mod}(t)$ or $T_e^{mod}(t)$, matches experimentally-observed results within a specified tolerance. Lehre et al. [16, 17] were the first to apply an implicit scheme to solve for the size distribution of a polydisperse aerosol using time-resolved LII data. Both Kuhlmann et al. [18] and Dankers and Leipertz [19] have also derived implicit techniques for finding particle size distributions using multivariate minimization. Liu et al. [20] describe an approach that transforms the multivariate minimization problem into an easier-to-solve univariate minimization problem. These techniques have been adopted by other researchers ([21–23], for example) to perform TR-LII aerosol particle sizing in a wide range of applications.

This paper surveys the implicit TR-LII particle sizing methods that have been presented in the literature. Each technique is described in detail and demonstrated by analyzing a set of artificial data generated using a specified size distri-

bution. Finally, a discussion of how the ill-posed nature of the inverse problem affects the accuracy of the recovered size distributions is presented, and the resilience of each particle-sizing method to uncertainties in the model parameters and experimental noise is assessed.

2 Test problem

The particle sizing techniques are demonstrated throughout this paper by using them to analyze an aerosol representative of in-flame soot. The particle diameters in many aerosols obey a lognormal probability density function,

$$f_d(d_p) = \frac{1}{d_p \sqrt{2\pi} \ln \sigma_g} \exp\left[-\left(\frac{\ln d_p/d_{pg}}{\sqrt{2} \ln \sigma_g} \right)^2 \right], \tag{8}$$

which has the corresponding cumulative distribution function

$$F_d(d_p) = \frac{1}{2}\left[1 + \mathrm{erf}\left(\frac{\ln d_p/d_{pg}}{2 \ln \sigma_g} \right) \right]. \tag{9}$$

Both of these functions are plotted in Fig. 1. The geometric mean, d_{pg}, and geometric standard deviation, σ_g, are set equal to 30 nm and 1.25, respectively, typical values for the primary particles of in-flame soot [20].

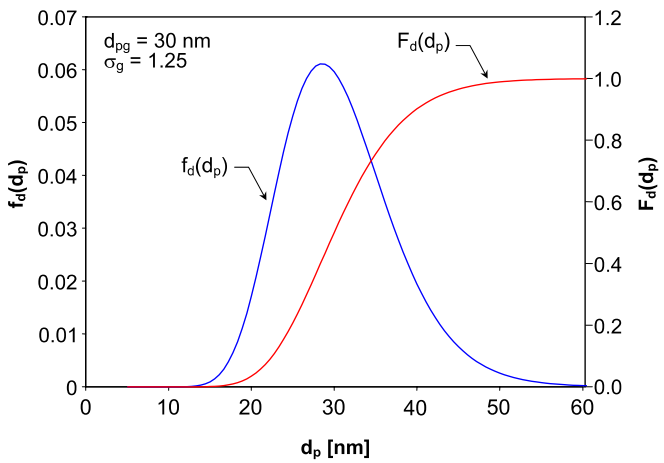

FIGURE 1 Lognormal particle size distribution

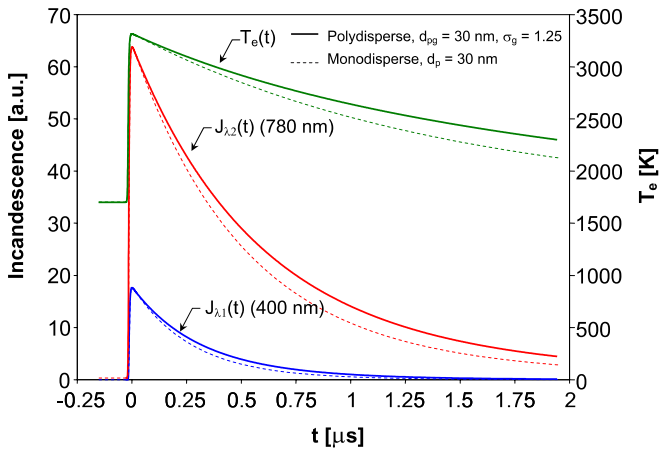

FIGURE 2 Simulated incandescence and effective temperature data

The spherical particles are heated from the ambient gas temperature, 1700 K, to a peak temperature of approximately 3300 K by the laser pulse and then cooled back to the ambient gas temperature. The time-dependent temperature of each particle size class is calculated by solving (1) using a fourth-order Runge–Kutta scheme. The thermal accommodation coefficient, α_T, is set equal to 0.3 and $E(\boldsymbol{m}_\lambda) = 0.3$ over all wavelengths. Temperature-dependent properties of the soot and flame gases are defined in a previous study [20].

The transient temperature distribution is then substituted into (5)–(7) to obtain simulated spectral incandescence measurements at $\lambda_1 = 400$ nm and $\lambda_2 = 780$ nm along with the derived effective temperature, which are plotted in Fig. 2. (Simulated data for a monodisperse aerosol with $d_p = 30$ nm is also plotted to show the effect of polydispersity on the LII signal.) A sampling interval of two nanoseconds is assumed, which is typical of many experiments.

3 Implicit solution schemes

Implicit solution schemes work by repeatedly solving the well-posed forward problem, i.e., determining the incandescence intensity or effective temperature decay corresponding to trial particle size distributions, until the predicted quantity, either $J_\lambda^{\mathrm{mod}}(t)$ or $T_e^{\mathrm{mod}}(t)$, matches the experimentally-observed one. The most efficient way to do this is to recast the problem as a least-squares minimization problem,

$$\min_{\boldsymbol{x}}[F(\boldsymbol{x})] = \min_{\boldsymbol{x}}\left[\frac{1}{2} \left\| \boldsymbol{b}^{\mathrm{exp}} - \boldsymbol{b}^{\mathrm{mod}}(\boldsymbol{x}) \right\|_2^2 \right], \tag{10}$$

where $F(\boldsymbol{x})$ is the objective function, the elements of $\boldsymbol{x}$ specify the particle size distribution, and $\boldsymbol{b}^{\mathrm{exp}}$ and $\boldsymbol{b}^{\mathrm{mod}}(\boldsymbol{x})$ contain the experimentally-observed and modeled data, respectively. In most soot-laden aerosols the primary particle diameters obey a log-normal distribution, so $\boldsymbol{x}$ is usually defined as $\boldsymbol{x} \equiv \{d_{pg}, \ln(\sigma_g)\}^{\mathrm{T}}$. (Using $\ln(\sigma_g)$ instead of σ_g improves the scaling of the minimization problem.) Nonlinear programming is then used to find the value of $\boldsymbol{x}^*$ that satisfies $F(\boldsymbol{x}^*) = \min[F(\boldsymbol{x})]$, which also defines the particle size distribution most likely to have produced the observed experimental data.

Nonlinear programming techniques work by minimizing $F(\boldsymbol{x})$ iteratively; at the kth iteration, the solution is updated by $\boldsymbol{x}^{k+1} = \boldsymbol{x}^k + \boldsymbol{p}^k \alpha^k$ where $\boldsymbol{p}^k$ is a search direction and α^k is a step size, which are both chosen based on the local topography of $F(\boldsymbol{x}^k)$. If $F(\boldsymbol{x})$ approximates a quadratic function in the vicinity of $\boldsymbol{x}^k$, the most efficient choice for $\boldsymbol{p}^k$ is Newton's direction [24],

$$\nabla^2 F(\boldsymbol{x}^k)\boldsymbol{p}^k = -\nabla F(\boldsymbol{x}^k)\,, \tag{11}$$

where the gradient vector and Hessian matrix contain first- and second-order objective function sensitivities, $\nabla F_p(\boldsymbol{x}^k) = \partial F(\boldsymbol{x}^k)/\partial x_p$ and $\nabla^2 F_{pq}(\boldsymbol{x}^k) = \partial^2 F(\boldsymbol{x}^k)/\partial x_p \partial x_q$, and α^k is set equal to unity. This approach, called Newton's method [24], usually requires the fewest iterations to find $\boldsymbol{x}$ of all the nonlinear programming methods (and only one step if $F(\boldsymbol{x})$ is a quadratic function of $\boldsymbol{x}$), although the computational effort needed to evaluate the second-order sensitivities make it unsuitable when $F(\boldsymbol{x})$ is expensive to calculate, which is

certainly the case in the present problem. Instead, in most least-squares objective functions the Hessian can be approximated accurately by $\nabla^2 F(\boldsymbol{x}^k) \approx \boldsymbol{J}^{\mathrm{T}}(\boldsymbol{x}^k)\boldsymbol{J}(\boldsymbol{x}^k)$, where $\boldsymbol{J}(\boldsymbol{x}^k)$ is the Jacobian of $\boldsymbol{f}(\boldsymbol{x})$, $J_{pq}(\boldsymbol{x}^k) = -\partial^2 b_p^{\mathrm{mod}}(\boldsymbol{x}^k)/\partial x_q$.

Unfortunately, in this problem both the Hessian and Jacobian are ill-conditioned in the vicinity of $\boldsymbol{x}^*$ due to the underlying ill-posedness of the problem; this condition can be diagnosed from the condition number of the Hessian matrix,

$$\mathrm{Cond}\left[\nabla^2 F(\boldsymbol{x}^k)\right] = \left\|\nabla^2 F(\boldsymbol{x}^k)\right\| / \left\|\nabla^2 F(\boldsymbol{x}^k)^{-1}\right\|, \tag{12}$$

with an equivalent expression applying for $\mathrm{Cond}[\boldsymbol{J}(\boldsymbol{x}^k)]$. A large value of $\mathrm{Cond}[\nabla^2 F(\boldsymbol{x}^k)]$ or $\mathrm{Cond}[\boldsymbol{J}(\boldsymbol{x}^k)]$ indicates that while there exists a unique search direction $\boldsymbol{p}^k$ that solves (11) exactly, there are also a large set of search directions, $\{\boldsymbol{p}^k\}$, that could also satisfy (11) with a small residual. The Levenburg–Marquardt method stabilizes the calculation of $\boldsymbol{p}^k$ by approximating the Hessian with $\nabla^2 F(\boldsymbol{x}^k) \approx \boldsymbol{J}^{\mathrm{T}}(\boldsymbol{x}^k)\boldsymbol{J}(\boldsymbol{x}^k) + \lambda^k \boldsymbol{I}$, where λ^k is a regularization parameter and $\boldsymbol{I}$ is the identity matrix; this dramatically reduces the number of search directions that "almost" solve (11). Most often Levenburg–Marquardt is implemented as a trust region method in which λ^k is defined implicitly through the size of the trust region, Δ^k, which forces $\|\boldsymbol{p}^k\|_2 \leq \Delta^k$ at each iteration [25]. The trust region size, in turn, is specified heuristically based on how closely $F(\boldsymbol{x})$ approximates a quadratic function in the vicinity of $\boldsymbol{x}^k$.

Although all implicit particle sizing techniques in the literature work by solving a least-squares minimization problem having the form of (11), each technique defines $F(\boldsymbol{x})$ in a different way. The first and most straightforward implementation was introduced by Lehre et al. [16], who defined $F(\boldsymbol{x})$ based on the difference between measured and modeled incandescence signals at m discrete observation times,

$$F(\boldsymbol{x}) = \frac{1}{2}\sum_{i=1}^{m}\left[J_\lambda^{\mathrm{exp}}(t_i) - J_\lambda^{\mathrm{mod}}(t_i, \boldsymbol{x})\right]^2, \tag{13}$$

and in a subsequent publication [17] effective temperature was substituted in place of monochromatic incandescence,

$$F(\boldsymbol{x}) = \frac{1}{2}\sum_{i=1}^{m}\left[T_{\mathrm{e}}^{\mathrm{exp}}(t_i) - T_{\mathrm{e}}^{\mathrm{mod}}(t_i, \boldsymbol{x})\right]^2. \tag{14}$$

Equations (13) and (14) are plotted in Fig. 3a and b, respectively.

Kuhlmann et al. [18] developed a more sophisticated approach based on the method of cumulants. If a distribution $f(\Gamma)$ is related to a measured signal $g(t)$ through a Laplacian integral equation,

$$g(t) = \int_0^\infty f(\Gamma)\exp(-\Gamma t)\,\mathrm{d}\Gamma \tag{15}$$

(a special type of Volterra equation of the first kind), then the exponential decay of $g(t)$ can be expressed as a power-series of t,

$$\ln[g(t)] = -K_1 t + \frac{K_2 t^2}{2} + \ldots + \frac{K_n(-t)^n}{n!}, \tag{16}$$

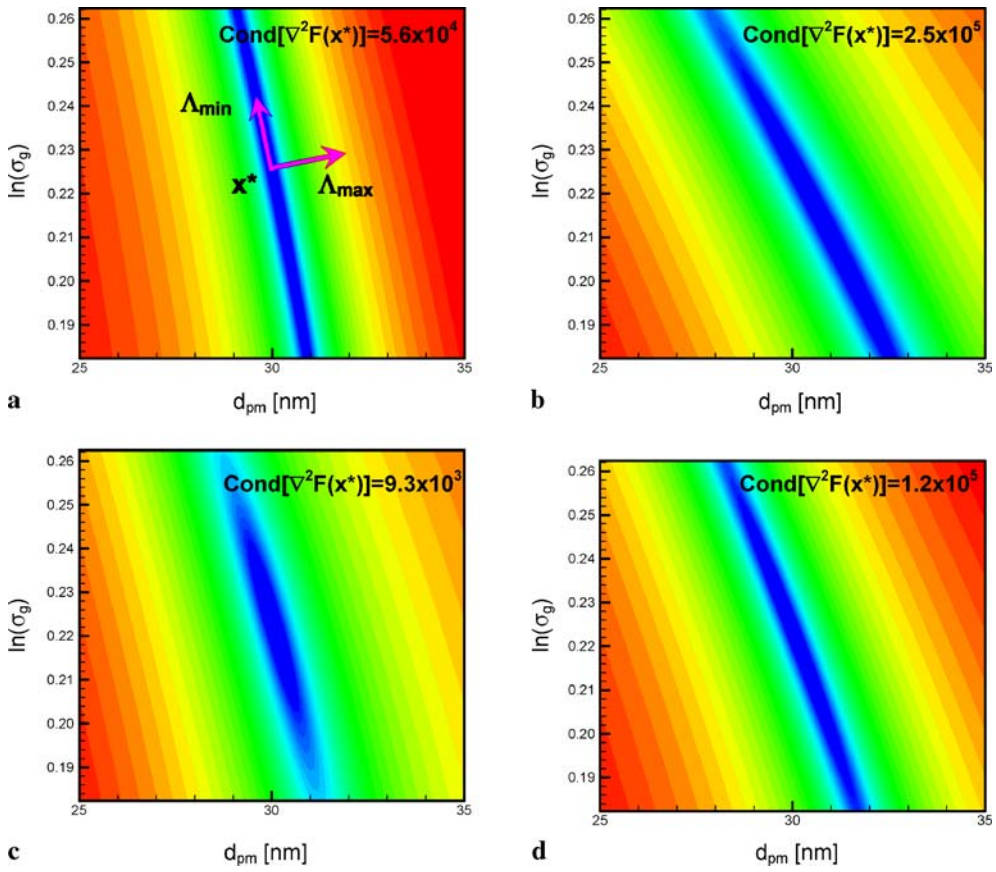

FIGURE 3 Least-squares objective functions used by different implicit solution techniques (**a**) (13), (**b**) (14), (**c**) (17), and (**d**) (18). Functions are normalized and are plotted on an exponential scale

where the coefficients $\{K_i, i = 1, 2, \dots\}$ are the cumulants of $f(\Gamma)$. If the distribution of Γ is log-normal, then $f(\Gamma)$ is defined completely by the first two cumulants, $2\sigma_g = K_2/K_1^2 + 1$ and $d_{pg} = K_1/2\sigma_g$. Unfortunately, this does not apply to Volterra integral equations of the first-kind in general, which can have more complicated kernels like (6). Instead, Kuhlmann et al. [18] derive cumulant-like parameters, K_1^{exp} and K_2^{exp}, from a quadratic regression of the log of experimentally measured monochromatic incandescence signals, $\{\ln[J_\lambda^{exp}(t_i)]\}$, following (16). The least-squared objective function is then defined as

$$F(\boldsymbol{x}) = \frac{1}{2}\left\{\left[K_1^{exp} - K_1^{mod}(\boldsymbol{x})\right]^2 + \left[K_2^{exp} - K_2^{mod}(x)\right]^2\right\}, \quad (17)$$

which is plotted in Fig. 3c.

Dankers and Leipertz [19] developed a similar method by fitting two exponential curves to the monochromatic incandescence signal over two different time domains, Δt_1 and Δt_2. The first time domain starts approximately 100 ns after the laser pulse and lasts 150–200 ns, while Δt_2 typically starts at 600 ns and lasts 200 ns provided the particles are sufficiently large and the ambient gas temperature is sufficiently high. The particle size distribution is then found by comparing the time constants of the exponential curves, τ_1^{exp} and τ_2^{exp}, to databases of model-generated time constants formed by varying d_{pg} and σ_g over a range of values. This is equivalent to minimizing

$$F(\boldsymbol{x}) = \frac{1}{2}\left\{\left[\tau_1^{exp} - \tau_1^{mod}(\boldsymbol{x})\right]^2 + \left[\tau_2^{exp} - \tau_2^{mod}(\boldsymbol{x})\right]^2\right\}, \quad (18)$$

which is plotted in Fig. 3d.

Although the above implicit methods all work by minimizing different objective functions, Fig. 3 shows that each of these functions is dominated by a long, shallow valley surrounding a strong local minimum at $\boldsymbol{x}^*$, which is characteristic of many objective functions that arise from ill-posed problems. Each objective function has at least one minimizer, $\boldsymbol{x}^*$, so Hadamard's first criterion requiring the existence of at least one solution is satisfied. Furthermore, Fig. 3 shows that the objective functions have only one minimizer, at least over the plotted range of d_{pg} and $\ln(\sigma_g)$, which means that Hadamard's second criterion demanding solution uniqueness is also satisfied. (Formal proofs of uniqueness must demonstrate that $F(\boldsymbol{x})$ is convex over the entire problem space, and are elusive if the objective function is complex.) The problem is ill-posed because any point along the floor of the valley surrounding $\boldsymbol{x}^*$ almost minimizes $F(\boldsymbol{x})$, i.e., it produces modeled data that closely resembles the experimentally observed data, even though it may specify an entirely different particle size distribution. Because of this, Hadamard's second criterion is almost violated, and as we will show later in the paper, Hadamard's third criterion is certainly violated.

This troublesome objective function topography is directly linked to the aforementioned ill-conditioning of the Hessian matrix at $\boldsymbol{x}^*$, since $\mathrm{Cond}[\nabla^2 F(\boldsymbol{x}^*)]$ approximates the ratio of the largest and smallest eigenvalues of the Hessian, $\Lambda_{max}/\Lambda_{min}$. These values, in turn, are the rates that $F(\boldsymbol{x})$ increases as $\boldsymbol{x}$ moves away from $\boldsymbol{x}^*$ in the directions of the corresponding Hessian eigenvectors, which point in the directions of maximum and minimum curvature of $F(\boldsymbol{x})$ at $\boldsymbol{x}^*$. The relationship between these parameters and the objective function topography is shown in Fig. 3a. Thus, a well-conditioned Hessian, $\mathrm{Cond}[\nabla^2 F(\boldsymbol{x}^*)] \approx 1$, indicates that the objective function is equally-curved in all directions while an ill-conditioned Hessian, $\mathrm{Cond}[\nabla^2 F(\boldsymbol{x}^*)] \gg 1$, is characteristic of the long, shallow valley surrounding $\boldsymbol{x}^*$.

A technique proposed by Liu et al. [20] further elucidates the ill-posed nature of the problem. It is based on the observation that, if the particles are heated to the same peak temperature at t_{max}, the initial effective temperature decay rate is governed by

$$\left.\frac{\mathrm{d}\ln(T_e - T_g)}{\mathrm{d}t}\right|_{t_{max}} = -\frac{C}{d_{p32}}, \quad (19)$$

where

$$C = \frac{3}{4}\frac{\alpha_T}{\varrho c}\frac{P_g \bar{c}}{T_g}\left(\frac{\gamma^* + 1}{\gamma^* - 1}\right), \quad (20)$$

and d_{p32} is the Sauter mean diameter,

$$d_{p32} = \int_0^\infty f_d(d_p) d_p^3 \,\mathrm{d}d_p \Big/ \int_0^\infty f_d(d_p) d_p^2 \,\mathrm{d}d_p, \quad (21)$$

which for a lognormal distribution is equal to

$$d_{p32} = d_{pg} \exp\left[5/2 \ln(\sigma_g)^2\right]. \quad (22)$$

Equations (19)–(22) provide a relationship between σ_g and d_{pg} and show that particle size distributions having the same Sauter mean diameter also have the same initial effective temperature decay after the laser pulse. At later times in the cooling process, however, the effective temperature decay rate becomes unique to a particular particle size distribution. In this approach, the first step is to calculate d_{p32} by performing a linear regression on a set of $\{\ln[T_e^{exp}(t_i) - T_g]\}$ data, where $t_{max} \le t_i \le t_{max} + 100$ ns. Once d_{p32} has been found, the lognormal size distribution is specified by only one parameter, say σ_g. The next step is to find the value of σ_g that causes the modeled effective temperature to match the measured effective temperature at some time t_c after the peak soot temperature, which can be done by minimizing

$$F(\sigma_g) = \left[T_e^{exp}(t_c) - T_e^{exp}(t_c, \sigma_g)\right]^2. \quad (23)$$

Liu et al. [20] found that for soot in flames at atmospheric pressure, the maximum sensitivity of $T_e(t_c)$ to σ_g was obtained by setting $t_c = 1.5$ µs; values of t_c for other scenarios can be determined from a sensitivity analysis. Figure 4 shows the curve $d_{p32} = d_{pg} \exp[5/2 \ln \sigma_g^2]$ plotted over the topography of (13) generated with $J_\lambda^{exp}(t_i)$ data collected between t_{max} and $t_{max} + 100$ ns. The Sauter mean curve corresponds to the floor of the valley surrounding $\boldsymbol{x}^*$ because different size distributions having the same d_{p32} produce similar incandescence curves. This is almost a violation of Hadamard's second criteria and causes a violation of Hadamard's third criterion, as demonstrated in the next section.

Recently, Stagg [26] suggested that the minimization problem can be stabilized by defining an objective function

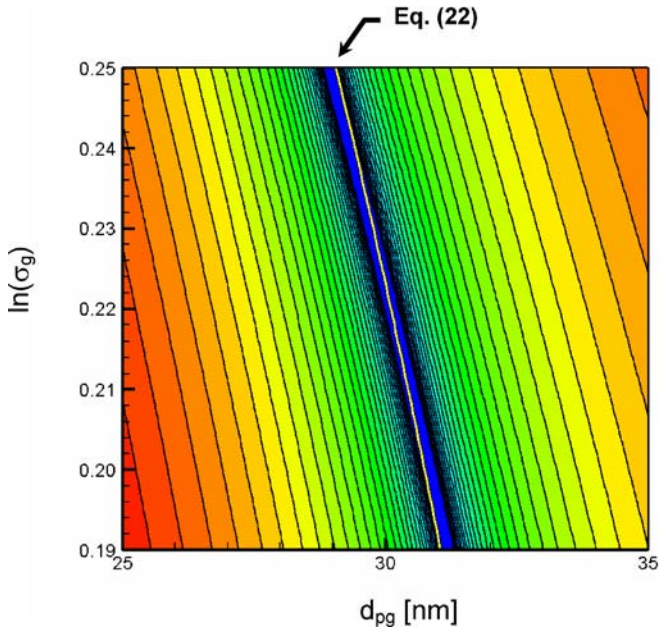

FIGURE 4 Equation (22) plotted over (14), generated using data measured up to 100 ns after the laser pulse

composed of two least-squares objective functions that have different principle curvature directions,

$$F(\boldsymbol{x}) = F_1(\boldsymbol{x}) + wF_2(\boldsymbol{x})\,, \tag{24}$$

where w is an adjustable weight. One possibility is to define $F_1(\boldsymbol{x})$ using (14) and let

$$F_2(\boldsymbol{x}) = \frac{1}{2}\left[\frac{\eta_2^{\exp}}{\eta_1^{\exp}} - \frac{\eta_2^{\mathrm{mod}}(\boldsymbol{x})}{\eta_1^{\mathrm{mod}}(\boldsymbol{x})}\right]^2, \tag{25}$$

where η_1 and η_2 are time constants similar to τ_1 and τ_2 used in (18), except they are found by fitting exponential curves to $T_{\mathrm{e}}(t) - T_{\mathrm{g}}$ instead of $J_\lambda(t)$. In this case, w was chosen to be 2×10^4 by minimizing $\mathrm{Cond}[\nabla^2 F(\boldsymbol{x}^*)]$. The three objective functions are plotted in Fig. 5. (Note that $F_1(\boldsymbol{x})$, $F_2(\boldsymbol{x})$, and $F(\boldsymbol{x})$ are all minimized by $\boldsymbol{x}^*$.) Figure 5a shows that the topography of $F_1(\boldsymbol{x})$ is dominated by a valley that roughly corresponds to the Sauter mean diameter and is almost perpendicular to the d_{pg} axis. In contrast, $F_2(\boldsymbol{x})$ is designed to emphasize the effective temperature decay rate at later cooling times, which more strongly depends on the particle size dispersion width, σ_{g}, instead of the mean particle diameter, d_{pg}, and accordingly, $F_2(\boldsymbol{x})$ has a valley that is roughly orthogonal to the valley of $F_1(\boldsymbol{x})$ as shown in Fig. 5b. (Note the differences between the effective temperature curves of monodisperse and polydisperse aerosols shown in Fig. 2.) Adding these two functions together produces a composite function that is steeper in the vicinity of $\boldsymbol{x}^*$ than both $F_1(\boldsymbol{x}^*)$ and $F_2(\boldsymbol{x}^*)$, and consequently a much smaller set of possible values of $\tilde{x}^*$ minimizes $F(\boldsymbol{x})$ within a given tolerance compared to both $F_1(\boldsymbol{x})$ and $F_2(\boldsymbol{x})$.

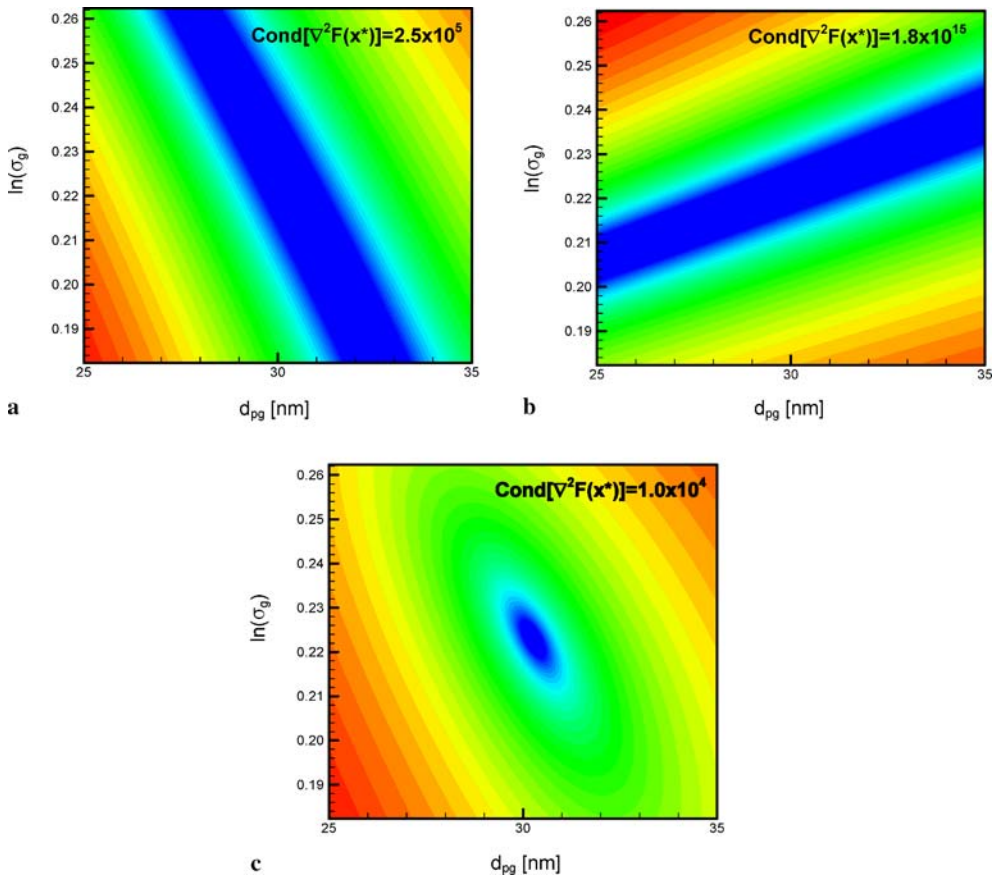

FIGURE 5 Adding (**a**) (14) to (**b**) (25) forms a composite objective function (**c**) that is steeper at $\boldsymbol{x}^*$

4 Solution accuracy and stability

In the previous section we showed that particle sizing through inverse analysis of time-resolved LII data involves solving an ill-posed problem that violates Hadamard's third criteria, and consequently we must expect the recovered particle size distribution to be highly sensitive to perturbations in the problem definition. In this problem, the perturbations are due to uncertainties in the model parameters and noise in the measured data.

4.1 *Model parameter uncertainty*

Many of the model parameters in time-resolved laser-induced incandescence studies are not known with a high degree of certainty, as recently highlighted by Schulz et al. [27] among others. In particular, the majority of LII studies on in-flame soot in the recent literature report values of α_T ranging from 0.23 to 0.37 [28] and wavelength-averaged values of $E(\boldsymbol{m})$ that range from 0.2 to 0.4 [29]. Lehre et al. [17] also suggest that particle sizing is sensitive to errors in gas temperature measurement, and even the most accurate in-flame measurements are subject to uncertainties of around 1–2%. (Although the observed incandescence decay in high-fluence LII experiments may be more sensitive to the particle size distribution compared to low-fluence experiments, this practice is not recommended for particle sizing due to the large model uncertainties associated particle evaporation, oxidation, and annealing [27, 30].)

The relative sensitivity of the size distributions recovered by the implicit techniques to model parameter uncertainties is assessed by performing a perturbation analysis. In this procedure, artificial monochromatic incandescence is first generated at 400 and 780 nm using the nominal model parameters, $\alpha_T = 0.3$, $E(\boldsymbol{m}) = 0.3$, and $T_g = 1700$ K, and the particle size distribution shown in Fig. 1. The six implicit techniques are then used to recover the particle size distribution from the artificial data, except the model parameters are perturbed to maximum and minimum values representative of the parameter uncertainties summarized in Table 1. In each case, the accuracy of the recovered distribution is quantified by the Cramér–von Mises (CVM) goodness-of-fit parameter [31], defined as the area contained between the recovered and exact particle size cumulative distribution functions,

$$[W(\boldsymbol{x})]^2 = \int_0^\infty \left[F_d(d_p, x) - F_d\left(d_p, x^*\right)\right]^2 \mathrm{d}d_p\,, \tag{26}$$

which is shown graphically in Fig. 6.

Model parameter	Nominal value	Perturbation
α_T	0.3	±0.05
$E(\boldsymbol{m}_\lambda)$	0.3	±0.1
T_g	1700 K	±30 K

TABLE 1 Nominal model parameters and perturbations

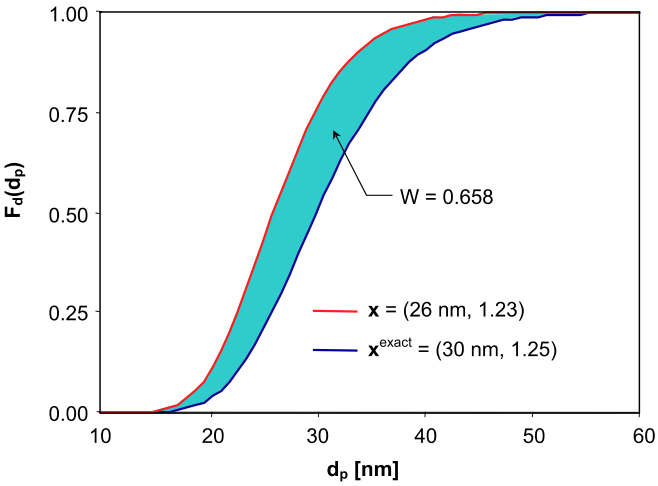

FIGURE 6 Graphical representation of the Cramér–von Mises goodness-of-fit statistic

The maximum CVM statistic associated with each perturbation is included in Table 2. The first column shows that the CVM statistics of the unperturbed recovered distributions are slightly larger than zero because the model used to calculate $J_\lambda^{mod}(\boldsymbol{x})$ and $T_e^{mod}(\boldsymbol{x})$ neglects residual laser heating after the peak temperature. (The method of Liu et al. [20] is particularly susceptible to this effect, since d_{p32} is calculated directly from data collected in the first 100 ns after the peak temperature.) In general, the recovered particle size distributions are most sensitive to accommodation coefficient perturbations; particle size distributions recovered using (14) with the perturbed accommodation coefficients are shown in Fig. 7. The composite technique is less sensitive than the other implicit schemes due to the influence of $F_2(\boldsymbol{x})$, which is relatively insensitive to the initial particle cooling rate. On the other hand, all methods are relatively insensitive to errors in T_g. The implicit methods based on effective temperature are completely insensitive to $E(\boldsymbol{m}_\lambda)$ as long as $E(\boldsymbol{m}_\lambda)$ is truly wavelength-independent, and the techniques derived by Kuhlmann et al. [18] and Dankers and Leipertz [19] are also resilient to uncertainties in $E(\boldsymbol{m}_\lambda)$. The least-squares monochromatic incandescence method of Lehre et al. [16] is very sensitive to $E(\boldsymbol{m}_\lambda)$, however.

The above analysis assumes that the peak particle temperature is measured directly using two-color pyrometry, and

Method	Nominal	$\alpha_T \pm 0.05$	$T_g \pm 30$ K	$E(\boldsymbol{m}_\lambda) \pm 0.1$
Lehre et al. [16]	0.014	1.206	0.280	1.812 (3.723)
Lehre et al. [17]	0.168	1.165	0.262	0.168
Kuhlmann et al. [18]	0.009	1.058	0.111	0.010 (1.388)
Dankers and Leipertz [19]	0.012	1.055	0.103	0.013 (1.101)
Liu et al. [20]	0.305	1.311	0.428	0.305
Composite, (24)	0.052	1.038	0.177	0.052

TABLE 2 Maximum CVM statistics due to model parameter uncertainty

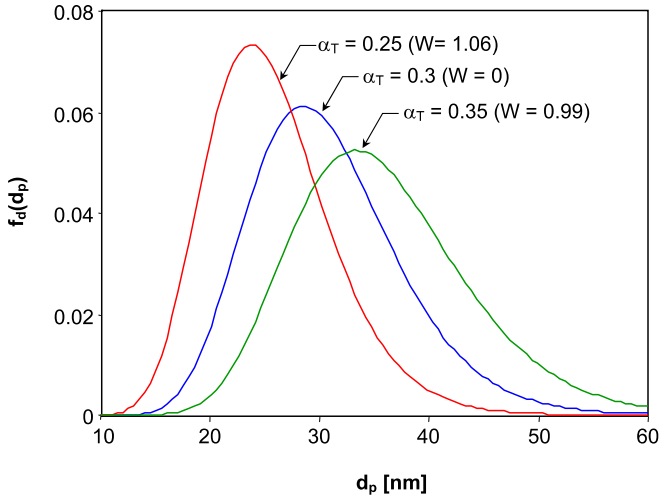

FIGURE 7 Effect of α_T uncertainty on size distributions recovered using (14)

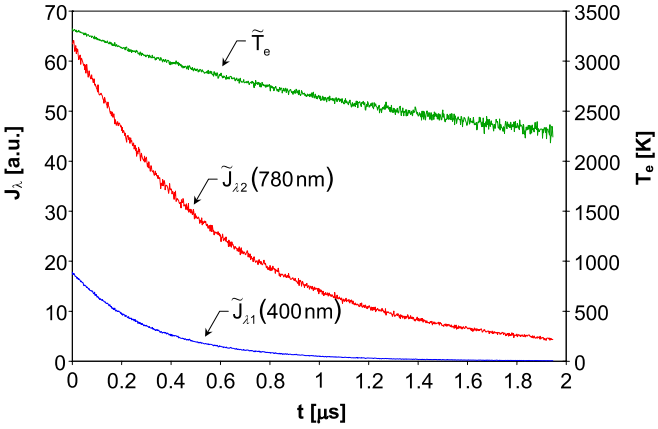

FIGURE 8 Synthetic 100-shot averaged LII data

that (1) does not include the laser excitation term. An alternative approach is to estimate the peak temperature by including the laser-excitation term in (1), which must be done if the probe volume incandescence is measured at only one wavelength. Uncertainties in $E(\boldsymbol{m}_\lambda)$ induce large errors in the estimated peak temperature, however, which in turn cause large errors in the recovered particle size distribution. The CVM statistics associated with this approach are included parenthetically in the $E(\boldsymbol{m}_\lambda)$ column of Table 2.

4.2 *Measurement uncertainty*

The sensitivity of the implicit solution methods to measurement noise was assessed by contaminating the synthetic incandescence signal with artificial photomultiplier shot noise according to

$$\tilde{J}_\lambda(t_i) = J_\lambda(t_i) + \varepsilon_\lambda(t_i)\,. \tag{27}$$

The time-dependent error, $\varepsilon_\lambda(t_i)$, is sampled from an unbiased Gaussian distribution having a standard deviation of $C_\lambda\sqrt{J_\lambda(t_i)}$ with C_λ set equal to 10% of the maximum signal strength of each channel, which is consistent with the operating theory of photodetectors [32] and typical of noise encountered in an experimental setting. The effect of photomultiplier shot noise is usually mitigated by averaging a large set of single-shot measurements, provided that the duration between measurements is small relative to the experimental time scale. (This procedure is easily implemented in experiments involving laminar diffusion flames, for example, but is more difficult for highly transient systems like in-cylinder measurements in internal combustion engines.) In this study, the replication process is simulated by taking the average of a large set of measurements generated independently using (27). The simulated 100-shot averaged LII data plotted in Fig. 8 shows that the signal quality degrades as the cooling time increases, which is characteristic of data collected in real LII experiments. It should be noted that photomultiplier shot noise in the averaged dataset is often obscured by noise caused by soot volume fraction fluctuations in the aerosol measurement volume, manifested as variations in incandescence signal magnitude between the single-shot measurements. This effect can be largely removed by normalizing each single-shot measurement individually.

The influence of objective function topography on error propagation is demonstrated in Fig. 9, which shows 40 solutions recovered from perturbed 100-shot averaged LII data using the method of Kuhlmann et al. [18] and plotted over the contours of the corresponding objective function. All the recovered solutions lie in the shallow valley surrounding $\boldsymbol{x}^*$. Even though the solutions are obtained from noise-contaminated LII signals closely resembling the unperturbed signal, they specify substantially different particle size distributions, as shown in the inset of Fig. 9.

The sensitivity of each implicit sizing technique to measurement noise is assessed by recovering particle size distributions from 40 independent sets of incandescence data, each in turn calculated by averaging different numbers of single-shot measurements. (Each method is applied to the same 40 independent sets of data.) The average CVM parameters are plotted in Fig. 10, and show that the method of Lehre et al. [16] based on monochromatic incandescence appear to be the most resilient to measurement noise, while the approach of Liu et al. [20] is the most sensitive. (One should keep in mind, however, that these results pertain to an artificial noise distribution typical of experimental data, and that different results may be obtained from different experimental data.)

The sensitivity of an implicit sizing technique to measurement noise depends on both the objective function curvature, given by $\mathrm{cond}[\nabla^2 F(\boldsymbol{x}^*)]$, and also the noise amplification caused by the variables used to define the least-squares objective function, which is quantified by the averaged, normalized standard deviation of the perturbed least-squares parameters,

$$\sigma_{b_i} = \|\delta\boldsymbol{b}\|_2/m\,, \tag{28}$$

where

$$\delta b_i = \left[\frac{1}{N}\sum_{i=1}^{N}\left(b_i/\bar{b}_i - 1\right)^2\right]^{1/2}, \tag{29}$$

m is the number of elements in $\boldsymbol{b}$, and N is the number of averaged single-shot measurements. Figure 11 shows that the least-squares parameters of the Lehre et al. [16, 17] methods cause very little noise amplification, while those of the Liu et

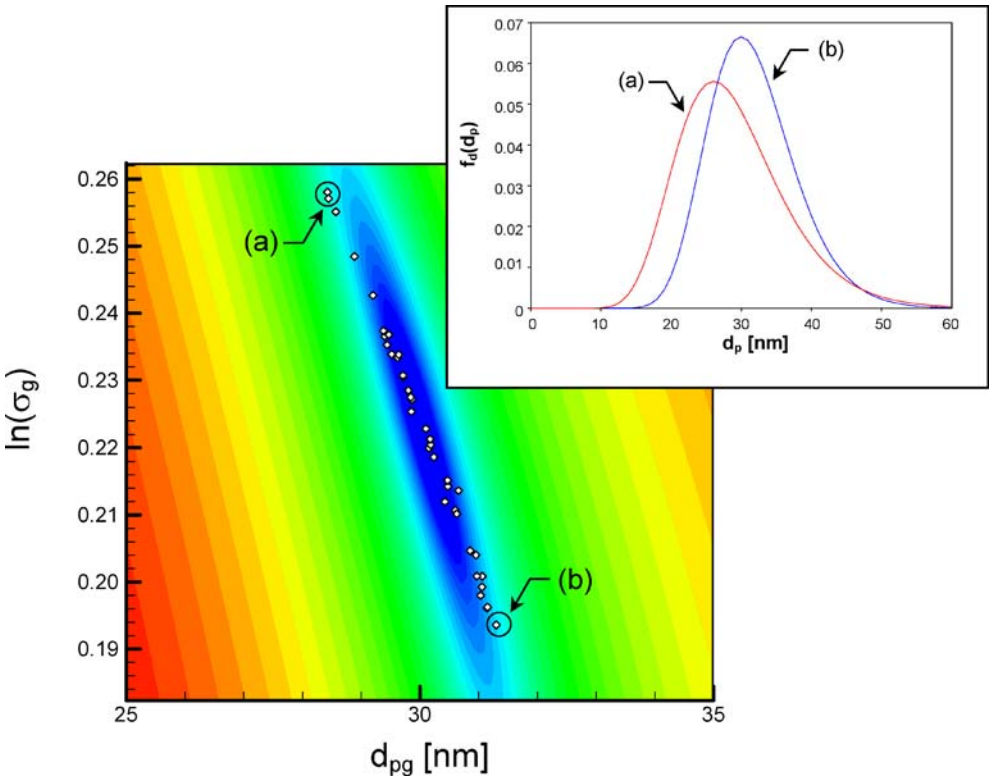

FIGURE 9 Solutions obtained using (17) and perturbed 100-shot averaged data. The *inset* shows size distributions corresponding to the two most extreme solutions

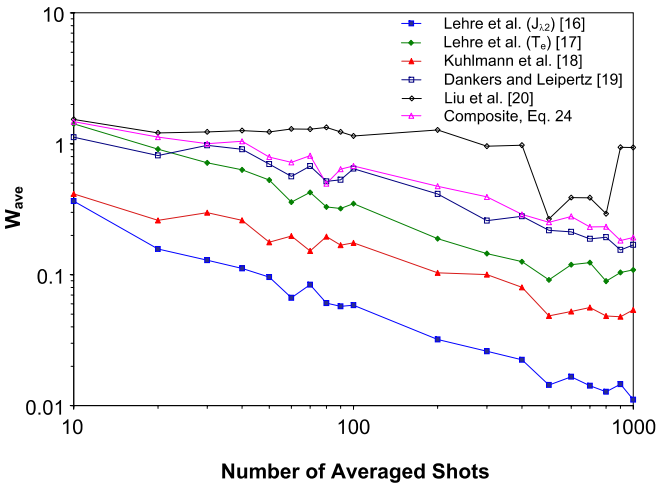

FIGURE 10 Relative sensitivity of the particle sizing techniques to measurement noise

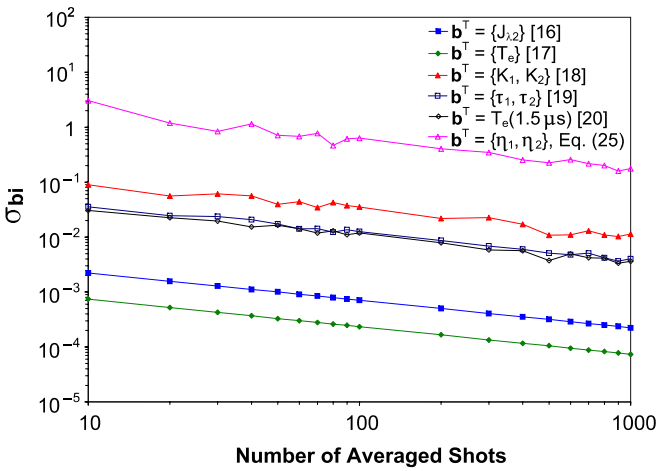

FIGURE 11 Noise amplification caused by least-squares objective function variables

al. method [20] and $F_2(\boldsymbol{x})$ of the composite objective function, (25), are particularly sensitive to measurement noise. In the case of the composite method, the noise generated by the $\{\eta_1, \eta_2\}^{\mathrm{T}}$ set of least-squares parameters completely negates the advantage of the increased objective function curvature at $\boldsymbol{x}^*$.

The most suitable method for recovering a particle size distribution depends on the characteristics of an individual experiment. If TR-LII is used to make instantaneous particle size measurements in highly transient systems, the number of single-shot measurements that can be made is limited and consequently the averaged LII signal tends to be noisy. In this scenario, using a particle sizing technique that is resilient to measurement noise, such as the methods of Lehre et al. [16, 17], is advisable. When making LII measurements on quasi steady-state systems, on the other hand, a large number of single shot measurements can be averaged to almost eliminate measurement noise. In this case the particle sizing technique should be chosen to minimize the error caused by model parameter uncertainty. Techniques based on two-color pyrometry [17, 20] are insensitive to uncertainty in $E(\boldsymbol{m}_\lambda)$, and the composite technique described above is less sensitive to uncertainty in α_{T} compared to the other methods.

5 Conclusions

Using time-resolved LII data to recover the particle size distribution in an aerosol is tantamount to solv-

ing an ill-posed inverse problem that violates Hadamard's third criterion. The most viable way of solving this problem is by first defining a least-squares objective function based on the difference between experimentally-observed and modeled data, which can then be minimized using nonlinear programming. The parameters that minimize the objective function specify the particle size distribution that most probably accounts for the experimentally-observed incandescence decay. Levenburg–Marquardt minimization is well-suited for carrying out the minimization since it addresses the ill-conditioning in the Hessian matrix of the objective function caused by the ill-posedness of the underlying inverse problem.

Because the inverse problem is ill-posed, recovered particle size distributions are sensitive to both model parameter uncertainty and measurement noise. Accordingly, when choosing an implicit particle sizing technique, it is important to consider the characteristics of a particular experiment. A perturbation analysis demonstrated that the size distribution is especially sensitive to uncertainties in the thermal accommodation coefficient, although the monochromatic incandescence-based method of Lehre et al. [16] and the composite method described in this paper are also highly sensitive to uncertainties in $E(\boldsymbol{m}_\lambda)$. The techniques of Lehre et al. [16, 17] are most robust to photodetector shot noise, while the approaches of Liu et al. [20] and the composite objective function are most sensitive to measurement noise.

REFERENCES

1 G. Oberdörster, E. Oberdörster, J. Oberdörster, Environ. Health Persp. **113**, 823 (2005)
2 M.Z. Jacobson, J. Geophys. Res. **107**, D19 (2002)
3 R. Viskanta, M.P. Menguç, Prog. Energ. Combust. Sci. **13**, 97 (1987)
4 S. Dankers, A. Leipertz, S. Will, J. Arndt, K. Vogel, S. Schraml, A. Hemm, Chem. Eng. Technol. **26**, 966 (2003)
5 L.A. Melton, Appl. Opt. **23**, 2202 (1984)
6 M. Kerker, *The Scattering of Light* (Academic Press, New York, 1969)
7 T.L. Farias, Ü.Ö. Köylu, M.G. Carvalho, Appl. Opt. **35**, 6560 (1996)
8 A.V. Filippov, D.E. Rosner, Int. J. Heat Mass Transf. **43**, 127 (2000)
9 A.V. Filippov, M. Zurita, D.E. Rosner, J. Colloid Interf. Sci. **229**, 261 (2000)
10 S. Will, S. Schraml, A. Leipertz, Opt. Lett. **20**, 2341 (1995)
11 B. Mewes, J.M. Seitzman, Appl. Opt. **36**, 709 (1997)
12 J. Hadamard, *Lectures on Cauchy's Problem in Linear Partial Differential Equations* (Yale University Press, New Haven, CT, 1923)
13 P. Roth, A.V. Filippov, J. Aerosol Sci. **27**, 95 (1996)
14 S. Twomey, J. Comput. Phys. **18**, 188 (1975)
15 G.R. Markowski, Aerosol Sci. Technol. **7**, 127 (1987)
16 T. Lehre, H. Bockhorn, B. Jungfleisch, R. Suntz, Chemosphere **51**, 1055 (2003)
17 T. Lehre, B. Jungfleisch, R. Suntz, H. Bockhorn, Appl. Opt. **42**, 2021 (2003)
18 S.A. Kuhlmann, J. Schumacher, J. Reimann, S. Will, Proc. PARTEC, Nuremburg, Germany, March 16–18, 2004
19 S. Dankers, A. Leipertz, Appl. Opt. **43**, 3726 (2004)
20 F. Liu, B.J. Stagg, D.R. Snelling, G.J. Smallwood, Int. J. Heat Mass Transf. **49**, 777 (2006)
21 T. Dreier, B. Bougie, N. Dam, T. Gerber, Appl. Phys. B **83**, 403 (2006)
22 B.F. Kock, P. Roth, Proc. European Combustion Meeting, Orléans, October 2003
23 B. Tribalet, B.F. Kock, P. Ifeacho, P. Roth, C. Schulz, Proc. 2nd Int. Meeting and Workshop on Laser-Induced Incandescence, Bad Herrenalb, August 2006
24 P.E. Gill, W. Murray, M.H. Wright, *Practical Optimization* (Academic Press, San Diego, CA, 1986)
25 J.J. More, D.C. Sorensen, SIAM J. Sci. Stat. Comput. **4**, 553 (1983)
26 B.J. Stagg, Proc. 2nd Int. Meeting and Workshop on Laser-Induced Incandescence, Bad Herrenalb, August 2006
27 C. Schulz, B.F. Kock, M. Hofmann, H. Michelsen, S. Will, B. Bougie, R. Suntz, G.J. Smallwood, Appl. Phys. B **83**, 333 (2006)
28 F. Liu, D.R. Snelling, G.J. Smallwood, Proc. 13th IHTC, Sydney, Australia, August 2006
29 F. Liu, K.J. Daun, G.J. Smallwood, 2nd Int. Meeting and Workshop on Laser-Induced Incandescence, Bad Herrenalb, Germany, August 2006
30 H.A. Michelsen, J. Chem. Phys. **118**, 15 (2003)
31 G.J. Smallwood, D.R. Snelling, F. Liu, Ö.L. Gülder, J. Heat Transf. **123** (2001)
32 R.B. D'Agostino, M.A. Stephens, *Goodness-of-fit Techniques* (Dekker, New York, 1986)
33 A. Yariv, *Introduction to Optical Electronics* (Holt, Reinhold and Winston, Inc., New York, 1971)